Research Article | Vol. 7, No. 12 | 1 Dec 2016 | BIOMEDICAL OPTICS EXPRESS 5218

Biomedical Optics EXPRESS

Depth-resolved imaging of colon tumor using optical coherence tomography and fluorescence laminar optical tomography

QINGGONG TANG,[1] JIANTING WANG,[1] AARON FRANK,[1] JONATHAN LIN,[1] ZHIFANG LI,[1,2] CHAO-WEI CHEN,[1] LILY JIN,[1] TONGTONG WU,[3] BRUCE D.GREENWALD,[4] HIROSHI MASHIMO,[5] AND YU CHEN[1,2,*]

[1]*Fischell Department of Bioengineering, University of Maryland, College Park, MD 20742, USA*
[2]*Key Laboratory of Optoelectronic Science and Technology for Medicine, Ministry of Education, College of Photonic and Electronic Engineering, Fujian Normal University, Fuzhou 350007, China*
[3]*Department of Biostatistics and Computational Biology, University of Rochester, Rochester, NY 14642, USA*
[4]*Division of Gastroenterology and Hepatology, University of Maryland School of Medicine, Baltimore, MD 21201, USA*
[5]*Department of Medicine, Veterans Affairs Boston Healthcare System, Harvard Medical School, West Roxbury, MA 02132, USA*
**yuchen@umd.edu*

Abstract: Early detection of neoplastic changes remains a critical challenge in clinical cancer diagnosis and treatment. Many cancers arise from epithelial layers such as those of the gastrointestinal (GI) tract. Current standard endoscopic technology is difficult to detect the subsurface lesions. In this research, we investigated the feasibility of a novel multi-modal optical imaging approach including high-resolution optical coherence tomography (OCT) and high-sensitivity fluorescence laminar optical tomography (FLOT) for structural and molecular imaging. The C57BL/6J-Apc^{Min}/J mice were imaged using OCT and FLOT, and the correlated histopathological diagnosis was obtained. Quantitative structural (scattering coefficient) and molecular (relative enzyme activity) parameters were obtained from OCT and FLOT images for multi-parametric analysis. This multi-modal imaging method has demonstrated the feasibility for more accurate diagnosis with 88.23% (82.35%) for sensitivity (specificity) compared to either modality alone. This study suggested that combining OCT and FLOT is promising for subsurface cancer detection, diagnosis, and characterization.

OCIS codes: (110.4190) Multiple imaging; (170.4500) Optical coherence tomography; (170.2520) Fluorescence microscopy; (170.3880) Medical and biological imaging

References and links

1. D. E. Fleischer, B. F. Overholt, V. K. Sharma, A. Reymunde, M. B. Kimmey, R. Chuttani, K. J. Chang, R. Muthasamy, C. J. Lightdale, N. Santiago, D. K. Pleskow, P. J. Dean, and K. K. Wang, "Endoscopic radiofrequency ablation for Barrett's esophagus: 5-year outcomes from a prospective multicenter trial," Endoscopy **42**(10), 781–789 (2010).
2. M. S. Dar, J. R. Goldblum, T. W. Rice, and G. W. Falk, "Can extent of high grade dysplasia in Barrett's oesophagus predict the presence of adenocarcinoma at oesophagectomy?" Gut **52**(4), 486–489 (2003).
3. N. J. Shaheen, A. F. Peery, B. F. Overholt, C. J. Lightdale, A. Chak, K. K. Wang, R. H. Hawes, D. E. Fleischer, J. R. Goldblum, and AIM Dysplasia Investigators, "Biopsy depth after radiofrequency ablation of dysplastic Barrett's esophagus," Gastrointest. Endosc. **72**(3), 490–496 (2010).
4. H. Mashimo, "Subsquamous intestinal metaplasia after ablation of Barrett's esophagus: frequency and importance," Curr. Opin. Gastroenterol. **29**(4), 454–459 (2013).
5. C. Zhou, T.-H. Tsai, H.-C. Lee, T. Kirtane, M. Figueiredo, Y. K. Tao, O. O. Ahsen, D. C. Adler, J. M. Schmitt, Q. Huang, J. G. Fujimoto, and H. Mashimo, "Characterization of buried glands before and after radiofrequency ablation by using 3-dimensional optical coherence tomography (with videos)," Gastrointest. Endosc. **76**(1), 32–40 (2012).
6. N. J. Shaheen, P. Sharma, B. F. Overholt, H. C. Wolfsen, R. E. Sampliner, K. K. Wang, J. A. Galanko, M. P. Bronner, J. R. Goldblum, A. E. Bennett, B. A. Jobe, G. M. Eisen, M. B. Fennerty, J. G. Hunter, D. E. Fleischer, V. K. Sharma, R. H. Hawes, B. J. Hoffman, R. I. Rothstein, S. R. Gordon, H. Mashimo, K. J. Chang, V. R.

#272105 http://dx.doi.org/10.1364/BOE.7.005218
Journal © 2016 Received 26 Jul 2016; revised 16 Nov 2016; accepted 16 Nov 2016; published 21 Nov 2016

Biomedical Optics EXPRESS

Muthusamy, S. A. Edmundowicz, S. J. Spechler, A. A. Siddiqui, R. F. Souza, A. Infantolino, G. W. Falk, M. B. Kimmey, R. D. Madanick, A. Chak, and C. J. Lightdale, "Radiofrequency ablation in Barrett's esophagus with dysplasia," N. Engl. J. Med. **360**(22), 2277–2288 (2009).
7. T.-H. Tsai, C. Zhou, Y. K. Tao, H.-C. Lee, O. O. Ahsen, M. Figueiredo, T. Kirtane, D. C. Adler, J. M. Schmitt, Q. Huang, J. G. Fujimoto, and H. Mashimo, "Structural markers observed with endoscopic 3-dimensional optical coherence tomography correlating with Barrett's esophagus radiofrequency ablation treatment response (with videos)," Gastrointest. Endosc. **76**(6), 1104–1112 (2012).
8. B. J. Vaccaro, S. Gonzalez, J. M. Poneros, P. D. Stevens, K. M. Capiak, C. J. Lightdale, and J. A. Abrams, "Detection of intestinal metaplasia after successful eradication of Barrett's Esophagus with radiofrequency ablation," Dig. Dis. Sci. **56**(7), 1996–2000 (2011).
9. R. E. Pouw, J. J. Gondrie, A. M. Rygiel, C. M. Sondermeijer, F. J. ten Kate, R. D. Odze, M. Vieth, K. K. Krishnadath, and J. J. Bergman, "Properties of the neosquamous epithelium after radiofrequency ablation of Barrett's esophagus containing neoplasia," Am. J. Gastroenterol. **104**(6), 1366–1373 (2009).
10. K. Ragunath, N. Krasner, V. S. Raman, M. T. Haqqani, C. J. Phillips, and I. Cheung, "Endoscopic ablation of dysplastic Barrett's oesophagus comparing argon plasma coagulation and photodynamic therapy: a randomized prospective trial assessing efficacy and cost-effectiveness," Scand. J. Gastroenterol. **40**(7), 750–758 (2005).
11. M. Mino-Kenudson, S. Ban, M. Ohana, W. Puricelli, V. Deshpande, M. Shimizu, N. S. Nishioka, and G. Y. Lauwers, "Buried dysplasia and early adenocarcinoma arising in barrett esophagus after porfimer-photodynamic therapy," Am. J. Surg. Pathol. **31**(3), 403–409 (2007).
12. N. A. Gray, R. D. Odze, and S. J. Spechler, "Buried metaplasia after endoscopic ablation of Barrett's esophagus: a systematic review," Am. J. Gastroenterol. **106**(11), 1899–1908 (2011).
13. M. Basavappa, A. Weinberg, Q. Huang, and H. Mashimo, "Markers suggest reduced malignant potential of subsquamous intestinal metaplasia compared with Barrett's esophagus," Dis. Esophagus **27**(3), 262–266 (2014).
14. D. Huang, E. A. Swanson, C. P. Lin, J. S. Schuman, W. G. Stinson, W. Chang, M. R. Hee, T. Flotte, K. Gregory, C. A. Puliafito, and et, "Optical coherence tomography," Science **254**(5035), 1178–1181 (1991).
15. J. G. Fujimoto, M. E. Brezinski, G. J. Tearney, S. A. Boppart, B. Bouma, M. R. Hee, J. F. Southern, and E. A. Swanson, "Optical biopsy and imaging using optical coherence tomography," Nat. Med. **1**(9), 970–972 (1995).
16. G. J. Tearney, M. E. Brezinski, B. E. Bouma, S. A. Boppart, C. Pitris, J. F. Southern, and J. G. Fujimoto, "In vivo endoscopic optical biopsy with optical coherence tomography," Science **276**(5321), 2037–2039 (1997).
17. B. E. Bouma, S. H. Yun, B. J. Vakoc, M. J. Suter, and G. J. Tearney, "Fourier-domain optical coherence tomography: recent advances toward clinical utility," Curr. Opin. Biotechnol. **20**(1), 111–118 (2009).
18. C. P. Liang, J. Wierwille, T. Moreira, G. Schwartzbauer, M. S. Jafri, C. M. Tang, and Y. Chen, "A forward-imaging needle-type OCT probe for image guided stereotactic procedures," Opt. Express **19**(27), 26283–26294 (2011).
19. J. Xi, A. Zhang, Z. Liu, W. Liang, L. Y. Lin, S. Yu, and X. Li, "Diffractive catheter for ultrahigh-resolution spectral-domain volumetric OCT imaging," Opt. Lett. **39**(7), 2016–2019 (2014).
20. G. K. Sharma, G. S. Ahuja, M. Wiedmann, K. E. Osann, E. Su, A. E. Heidari, J. C. Jing, Y. Qu, F. Lazarow, A. Wang, L. Chou, C. C. Uy, V. Dhar, J. P. Cleary, N. Pham, K. Huoh, Z. Chen, and B. J. F. Wong, "Long-Range Optical Coherence Tomography of the Neonatal Upper Airway for Early Diagnosis of Intubation-related Subglottic Injury," Am. J. Respir. Crit. Care Med. **192**(12), 1504–1513 (2015).
21. Y. Chen, A. D. Aguirre, P. L. Hsiung, S. Desai, P. R. Herz, M. Pedrosa, Q. Huang, M. Figueiredo, S. W. Huang, A. Koski, J. M. Schmitt, J. G. Fujimoto, and H. Mashimo, "Ultrahigh resolution optical coherence tomography of Barrett's esophagus: preliminary descriptive clinical study correlating images with histology," Endoscopy **39**(7), 599–605 (2007).
22. A. Sergeev, V. Gelikonov, G. Gelikonov, F. Feldchtein, R. Kuranov, N. Gladkova, N. Shakhova, L. Snopova, A. Shakhov, I. Kuznetzova, A. Denisenko, V. Pochinko, Y. Chumakov, and O. Streltzova, "In vivo endoscopic OCT imaging of precancer and cancer states of human mucosa," Opt. Express **1**(13), 432–440 (1997).
23. B. E. Bouma, G. J. Tearney, C. C. Compton, and N. S. Nishioka, "High-resolution imaging of the human esophagus and stomach in vivo using optical coherence tomography," Gastrointest. Endosc. **51**(4), 467–474 (2000).
24. M. J. Gora, J. S. Sauk, R. W. Carruth, K. A. Gallagher, M. J. Suter, N. S. Nishioka, L. E. Kava, M. Rosenberg, B. E. Bouma, and G. J. Tearney, "Tethered capsule endomicroscopy enables less invasive imaging of gastrointestinal tract microstructure," Nat. Med. **19**(2), 238–240 (2013).
25. J. M. Poneros, S. Brand, B. E. Bouma, G. J. Tearney, C. C. Compton, and N. S. Nishioka, "Diagnosis of specialized intestinal metaplasia by optical coherence tomography," Gastroenterology **120**(1), 7–12 (2001).
26. K. Liang, G. Traverso, H. C. Lee, O. O. Ahsen, Z. Wang, B. Potsaid, M. Giacomelli, V. Jayaraman, R. Barman, A. Cable, H. Mashimo, R. Langer, and J. G. Fujimoto, "Ultrahigh speed en face OCT capsule for endoscopic imaging," Biomed. Opt. Express **6**(4), 1146–1163 (2015).
27. G. Isenberg, M. V. Sivak, Jr., A. Chak, R. C. K. Wong, J. E. Willis, B. Wolf, D. Y. Rowland, A. Das, and A. Rollins, "Accuracy of endoscopic optical coherence tomography in the detection of dysplasia in Barrett's esophagus: a prospective, double-blinded study," Gastrointest. Endosc. **62**(6), 825–831 (2005).
28. J. A. Evans, J. M. Poneros, B. E. Bouma, J. Bressner, E. F. Halpern, M. Shishkov, G. Y. Lauwers, M. Mino-Kenudson, N. S. Nishioka, and G. J. Tearney, "Optical coherence tomography to identify intramucosal carcinoma and high-grade dysplasia in Barrett's esophagus," Clin. Gastroenterol. Hepatol. **4**(1), 38–43 (2006).

Biomedical Optics EXPRESS

29. Z. G. Wang, D. B. Durand, M. Schoenberg, and Y. T. Pan, "Fluorescence guided optical coherence tomography for the diagnosis of early bladder cancer in a rat model," J. Urol. **174**(6), 2376–2381 (2005).
30. V. V. Sapozhnikova, N. M. Shakhova, V. A. Kamensky, S. A. Petrova, L. B. Snopova, and R. V. Kuranov, "Capabilities of fluorescence spectroscopy using 5-ALA and optical coherence tomography for diagnosis of neoplastic processes in the uterine cervix and vulva," Laser Phys. **15**, 1664–1673 (2005).
31. R. V. Kuranov, V. V. Sapozhnikova, H. M. Shakhova, V. M. Gelikonov, E. V. Zagainova, and S. A. Petrova, "Combined application of optical methods to increase the information content of optical coherent tomography in diagnostics of neoplastic processes," Quantum Electron. **32**(11), 993–998 (2002).
32. Y. T. Pan, T. Q. Xie, C. W. Du, S. Bastacky, S. Meyers, and M. L. Zeidel, "Enhancing early bladder cancer detection with fluorescence-guided endoscopic optical coherence tomography," Opt. Lett. **28**(24), 2485–2487 (2003).
33. A. R. Tumlinson, J. K. Barton, B. Povazay, H. Sattman, A. Unterhuber, R. A. Leitgeb, and W. Drexler, "Endoscope-tip interferometer for ultrahigh resolution frequency domain optical coherence tomography in mouse colon," Opt. Express **14**(5), 1878–1887 (2006).
34. A. R. Tumlinson, L. P. Hariri, U. Utzinger, and J. K. Barton, "Miniature endoscope for simultaneous optical coherence tomography and laser-induced fluorescence measurement," Appl. Opt. **43**(1), 113–121 (2004).
35. L. P. Hariri, A. R. Tumlinson, D. G. Besselsen, U. Utzinger, E. W. Gerner, and J. K. Barton, "Endoscopic optical coherence tomography and laser-induced fluorescence spectroscopy in a murine colon cancer model," Lasers Surg. Med. **38**(4), 305–313 (2006).
36. S. Lam, B. Standish, C. Baldwin, A. McWilliams, J. leRiche, A. Gazdar, A. I. Vitkin, V. Yang, N. Ikeda, and C. MacAulay, "In vivo optical coherence tomography imaging of preinvasive bronchial lesions," Clin. Cancer Res. **14**(7), 2006–2011 (2008).
37. W. Yu, R. M. Sandoval, and B. A. Molitoris, "Rapid determination of renal filtration function using an optical ratiometric imaging approach," Am. J. Physiol. Renal Physiol. **292**(6), F1873–F1880 (2007).
38. V. E. Centonze and J. G. White, "Multiphoton excitation provides optical sections from deeper within scattering specimens than confocal imaging," Biophys. J. **75**(4), 2015–2024 (1998).
39. V. Ntziachristos, C. H. Tung, C. Bremer, and R. Weissleder, "Fluorescence molecular tomography resolves protease activity in vivo," Nat. Med. **8**(7), 757–761 (2002).
40. E. M. C. Hillman, O. Bernus, E. Pease, M. B. Bouchard, and A. Pertsov, "Depth-resolved optical imaging of transmural electrical propagation in perfused heart," Opt. Express **15**(26), 17827–17841 (2007).
41. E. M. C. Hillman, D. A. Boas, A. M. Dale, and A. K. Dunn, "Laminar optical tomography: demonstration of millimeter-scale depth-resolved imaging in turbid media," Opt. Lett. **29**(14), 1650–1652 (2004).
42. Q. Tang, V. Tsytsarev, A. Frank, Y. Wu, C. W. Chen, R. S. Erzurumlu, and Y. Chen, "In Vivo Mesoscopic Voltage-Sensitive Dye Imaging of Brain Activation," Sci. Rep. **6**, 25269 (2016).
43. A. Dunn and D. Boas, "Transport-based image reconstruction in turbid media with small source-detector separations," Opt. Lett. **25**(24), 1777–1779 (2000).
44. B. Yuan, S. A. Burgess, A. Iranmahboob, M. B. Bouchard, N. Lehrer, C. Bordier, and E. M. C. Hillman, "A system for high-resolution depth-resolved optical imaging of fluorescence and absorption contrast," Rev. Sci. Instrum. **80**(4), 043706 (2009).
45. S. Yuan, Q. Li, J. Jiang, A. Cable, and Y. Chen, "Three-dimensional coregistered optical coherence tomography and line-scanning fluorescence laminar optical tomography," Opt. Lett. **34**(11), 1615–1617 (2009).
46. T. J. Muldoon, S. A. Burgess, B. R. Chen, D. Ratner, and E. M. C. Hillman, "Analysis of skin lesions using laminar optical tomography," Biomed. Opt. Express **3**(7), 1701–1712 (2012).
47. Y. Chen, S. Yuan, J. Wierwille, R. Naphas, Q. A. Li, T. R. Blackwell, P. T. Winnard, V. Raman, and K. Glunde, "Integrated Optical Coherence Tomography (OCT) and Fluorescence Laminar Optical Tomography (FLOT)," IEEE J. Sel. Top. Quant **16**(4), 755–766 (2010).
48. M. S. Ozturk, C. W. Chen, R. Ji, L. Zhao, B. N. B. Nguyen, J. P. Fisher, Y. Chen, and X. Intes, "Mesoscopic Fluorescence Molecular Tomography for Evaluating Engineered Tissues," Ann. Biomed. Eng. **44**(3), 667–679 (2016).
49. M. S. Ozturk, D. Rohrbach, U. Sunar, and X. Intes, "Mesoscopic fluorescence tomography of a photosensitizer (HPPH) 3D biodistribution in skin cancer," Acad. Radiol. **21**(2), 271–280 (2014).
50. Q. Tang, J. Lin, V. Tsytsarev, R. S. Erzurumlu, Y. Liu, and Y. Chen, "Review of mesoscopic optical tomography for depth-resolved imaging of hemodynamic changes and neural activities," Neurophotonics **4**(1), 011009 (2016).
51. H. S. Wasan, M. Novelli, J. Bee, and W. F. Bodmer, "Dietary fat influences on polyp phenotype in multiple intestinal neoplasia mice," Proc. Natl. Acad. Sci. U.S.A. **94**(7), 3308–3313 (1997).
52. C. Bremer, V. Ntziachristos, B. Weitkamp, G. Theilmeier, W. Heindel, and R. Weissleder, "Optical imaging of spontaneous breast tumors using protease sensing 'smart' optical probes," Invest. Radiol. **40**(6), 321–327 (2005).
53. K. Marten, C. Bremer, K. Khazaie, M. Sameni, B. Sloane, C. H. Tung, and R. Weissleder, "Detection of dysplastic intestinal adenomas using enzyme-sensing molecular beacons in mice," Gastroenterology **122**(2), 406–414 (2002).
54. Z. Ding, C. P. Liang, Q. Tang, and Y. Chen, "Quantitative single-mode fiber based PS-OCT with single input polarization state using Mueller matrix," Biomed. Opt. Express **6**(5), 1828–1843 (2015).
55. Z. Ding, Q. Tang, C.-P. Liang, K. Wu, A. Sandlerc, H. Li, and Y. Chen, "Imaging Spinal Structures With Polarization-Sensitive Optical Coherence Tomography," IEEE Photonics J. **8**, 1–8 (2016).

Biomedical Optics EXPRESS

56. Q. Tang, C.-P. Liang, K. Wu, A. Sandler, and Y. Chen, "Real-time epidural anesthesia guidance using optical coherence tomography needle probe," Quant. Imaging Med. Surg. **5**(1), 118–124 (2015).
57. Q. Tang, V. Tsytsarev, C. P. Liang, F. Akkentli, R. S. Erzurumlu, and Y. Chen, "In Vivo Voltage-Sensitive Dye Imaging of Subcortical Brain Function," Sci. Rep. **5**, 17325 (2015).
58. S. Yuan, Q. Li, J. Jiang, A. Cable, and Y. Chen, "Three-dimensional coregistered optical coherence tomography and line-scanning fluorescence laminar optical tomography," Opt. Lett. **34**(11), 1615–1617 (2009).
59. S. Yuan, C. A. Roney, J. Wierwille, C. W. Chen, B. Xu, G. Griffiths, J. Jiang, H. Ma, A. Cable, R. M. Summers, and Y. Chen, "Co-registered optical coherence tomography and fluorescence molecular imaging for simultaneous morphological and molecular imaging," Phys. Med. Biol. **55**(1), 191–206 (2010).
60. C. W. Chen and Y. Chen, "Optimization Of Design Parameters for Fluorescence Laminar Optical Tomography," J. Innov. Opt. Health Sci. **4**(3), 309–323 (2011).
61. L. Wang and S. L. Jacques, "Use of a laser beam with an oblique angle of incidence to measure the reduced scattering coefficient of a turbid medium," Appl. Opt. **34**(13), 2362–2366 (1995).
62. J. Huisken, J. Swoger, F. Del Bene, J. Wittbrodt, and E. H. K. Stelzer, "Optical sectioning deep inside live embryos by selective plane illumination microscopy," Science **305**(5686), 1007–1009 (2004).
63. Q. Fang and D. A. Boas, "Monte Carlo simulation of photon migration in 3D turbid media accelerated by graphics processing units," Opt. Express **17**(22), 20178–20190 (2009).
64. J. P. Culver, V. Ntziachristos, M. J. Holboke, and A. G. Yodh, "Optimization of optode arrangements for diffuse optical tomography: A singular-value analysis," Opt. Lett. **26**(10), 701–703 (2001).
65. P. C. Hansen and D. P. O'Leary, "The use of the L-curve in the regularization of discrete ill-posed problems," SIAM J. Sci. Comput. **14**(6), 1487–1503 (1993).
66. M. T. Tsai, H. C. Lee, C. K. Lee, C. H. Yu, H. M. Chen, C. P. Chiang, C. C. Chang, Y. M. Wang, and C. C. Yang, "Effective indicators for diagnosis of oral cancer using optical coherence tomography," Opt. Express **16**(20), 15847–15862 (2008).
67. M. T. Tsai, H. C. Lee, C. W. Lu, Y. M. Wang, C. K. Lee, C. C. Yang, and C. P. Chiang, "Delineation of an oral cancer lesion with swept-source optical coherence tomography," J. Biomed. Opt. **13**(4), 044012 (2008), doi:10.1117/1.2960632.
68. B. D. Goldberg, N. V. Iftimia, J. E. Bressner, M. B. Pitman, E. Halpern, B. E. Bouma, and G. J. Tearney, "Automated algorithm for differentiation of human breast tissue using low coherence interferometry for fine needle aspiration biopsy guidance," J. Biomed. Opt. **13**(1), 014014 (2008), doi:10.1117/1.2837433.
69. M. Mujat, R. D. Ferguson, D. X. Hammer, C. Gittins, and N. Iftimia, "Automated algorithm for breast tissue differentiation in optical coherence tomography," J. Biomed. Opt. **14**(3), 034040 (2009), doi:10.1117/1.3156821.
70. D. Levitz, L. Thrane, M. Frosz, P. Andersen, C. Andersen, S. Andersson-Engels, J. Valanciunaite, J. Swartling, and P. Hansen, "Determination of optical scattering properties of highly-scattering media in optical coherence tomography images," Opt. Express **12**(2), 249–259 (2004).
71. W. F. Cheong, S. A. Prahl, and A. J. Welch, "A Review Of the Optical-Properties Of Biological Tissues," IEEE J. Quantum Electron. **26**(12), 2166–2185 (1990).
72. P. R. Pfau, M. V. Sivak, Jr., A. Chak, M. Kinnard, R. C. K. Wong, G. A. Isenberg, J. A. Izatt, A. Rollins, and V. Westphal, "Criteria for the diagnosis of dysplasia by endoscopic optical coherence tomography," Gastrointest. Endosc. **58**(2), 196–202 (2003).
73. R. A. Burrell, N. McGranahan, J. Bartek, and C. Swanton, "The causes and consequences of genetic heterogeneity in cancer evolution," Nature **501**(7467), 338–345 (2013).
74. A. Swager, D. Boerwinkel, D. Bruin, B. Weusten, D. Faber, S. Meijer, T. Leeuwen, W. Curvers, and J. Bergman, "Volumetric laser endomicroscopy in Barrett's esophagus: a feasibility study on histological correlation," Dis. Esophagus **29**(6), 505–512 (2015).
75. D. A. Boas, C. Pitris, and N. Ramanujam, *Handbook of Biomedical Optics* (CRC press, 2011).
76. S. L. Jacques, "Optical properties of biological tissues: a review," Phys. Med. Biol. **58**(11), R37–R61 (2013).
77. M. F. Wood, N. Vurgun, M. A. Wallenburg, and I. A. Vitkin, "Effects of formalin fixation on tissue optical polarization properties," Phys. Med. Biol. **56**(8), N115–N122 (2011).
78. P.-L. Hsiung, P. R. Nambiar, and J. G. Fujimoto, "Effect of tissue preservation on imaging using ultrahigh resolution optical coherence tomography," J. Biomed. Opt. **10**(6), 064033 (2005).
79. X. Chen, Y. Hou, M. Tohme, R. Park, V. Khankaldyyan, I. Gonzales-Gomez, J. R. Bading, W. E. Laug, and P. S. Conti, "Pegylated Arg-Gly-Asp peptide: 64Cu labeling and PET imaging of brain tumor alphavbeta3-integrin expression," J. Nucl. Med. **45**(10), 1776–1783 (2004).
80. G. M. van Dam, G. Themelis, L. M. Crane, N. J. Harlaar, R. G. Pleijhuis, W. Kelder, A. Sarantopoulos, J. S. de Jong, H. J. Arts, A. G. van der Zee, J. Bart, P. S. Low, and V. Ntziachristos, "Intraoperative tumor-specific fluorescence imaging in ovarian cancer by folate receptor-α targeting: first in-human results," Nat. Med. **17**(10), 1315–1319 (2011).
81. M. Li, C. P. Anastassiades, B. Joshi, C. M. Komarck, C. Piraka, B. J. Elmunzer, D. K. Turgeon, T. D. Johnson, H. Appelman, D. G. Beer, and T. D. Wang, "Affinity peptide for targeted detection of dysplasia in Barrett's esophagus," Gastroenterology **139**(5), 1472–1480 (2010).
82. T. Xie, D. Mukai, S. Guo, M. Brenner, and Z. Chen, "Fiber-optic-bundle-based optical coherence tomography," Opt. Lett. **30**(14), 1803–1805 (2005).
83. M. Süzen, A. Giannoula, and T. Durduran, "Compressed sensing in diffuse optical tomography," Opt. Express **18**(23), 23676–23690 (2010).

Biomedical Optics EXPRESS

1. Introduction

Early detection of neoplastic changes remains a critical challenge in clinical cancer diagnosis and treatment. Many cancers arise from epithelial layers such as those of the gastrointestinal (GI) tract. White-light endoscopy guided excisional biopsy and histopathology is currently the gold standard for GI cancer diagnosis. However, it suffers from high false negative rates due to sampling errors [1–4]. Furthermore, a significant portion of patients after endoscopic ablative therapeutic treatment showed the presence of metaplasia or dysplasia buried underneath the neo-epithelium [5–9], which is associated with the risk of cancer development [4, 10–13]. Current standard endoscopic technology is unable to detect those subsurface lesions. Therefore, there is a critical need for developing new diagnostic tools which can assess tissue architectural and molecular information across the mucosal depth for improved detection of subsurface cancer, and evaluate the invasion depth of a lesion.

Optical coherence tomography (OCT) is an established biomedical imaging technology for subsurface imaging of tissues with high resolution (<10 μm) and 1-2 mm penetration depth [14–17], which is comparable to the size of standard pinch biopsy and histology. OCT can be interfaced with fiber-optic catheters and endoscopes to image inside the body [16, 18–20]. Endoscopic OCT has been demonstrated in the human GI tract [21–24] to detect Barrett's esophagus (BE) [25, 26] and dysplasia [27, 28]. OCT's high depth-resolution and appropriate penetration depth make it an attractive technology for detecting subsurface abnormalities in the mucosal and submucosal layers. Visualization of cross-sectional mucosal and submucosal features is a key advantage of OCT imaging when compared to standard endoscopy.

OCT can provide high-resolution morphology information, but is less sensitive to biochemical or molecular processes associated with early neoplastic formation before the exhibition of structural alterations. Fluorescence imaging has high sensitivity for detecting biochemical and molecular alterations, but has limited specificity [29]. Combining these two complementary imaging technologies would potentially improve the diagnostic capability for early cancer detection. Previous studies using OCT and depth-integrated fluorescence imaging already showed substantial promises in cervical [30, 31], bladder [29, 32], colorectal [33–35], and bronchial cancers [36]. However, depth-integrated fluorescence imaging lacks the depth-resolved information, therefore may not sufficiently indicate the subsurface lesions or estimate the depth-extent of the lesions. In addition, the detected fluorescence intensities are non-linearly attenuated with different imaging depths [37–39], which could lead to a surface weighted images.

Laminar optical tomography (LOT) is a promising approach to overcome this limitation by using multiple detectors to collect lights travelling through different depths, and through mathematical de-convolution to reconstruct the depth-resolved image [40–42]. LOT has a resolution of ~100 μm with 2-3 mm penetration depths [40–45], which is comparable to the imaging depth of OCT, as well as the size of typical biopsy and histology. LOT imaging of skin cancer based on absorption contrast has been demonstrated [46]. Fluorescence-based LOT (FLOT) has the potential to quantify depth-resolved distribution of fluorescence-labeled tumor [47–50].

Since cancer development is associated with both morphological and molecular alterations, imaging technologies that can quantitative image tissue's morphological and molecular biomarkers and assess the depth extent of a lesion, without the need for tissue excision, would be a major advance in cancer diagnostics and therapy. In this paper, we investigated multi-modal depth-resolved imaging approach by co-registering high-resolution OCT and high-sensitivity FLOT for both structural and molecular imaging. Our data on multi-modal imaging of mice colon tumor model demonstrated the feasibility of combining structural and molecular information for more accurate diagnosis.

Biomedical Optics EXPRESS

2. Materials and methods

2.1 Animal preparation

All animal procedures were approved by the Institutional Animal Care and Use Committee (IACUC) at the University of Maryland, and animals were treated in accordance with the PHS Policy on Humane Care and Use of Laboratory Animals, the National Institutes of Health Guide for the Care and Use of Laboratory Animals, and the Animal Welfare Act (7 U.S.C. et seq.). Six 8-week-old male C57BL/6J-Apc^{Min}/J mice were purchased from Jackson Laboratory (Bar Harbor, ME). The mice received a high fat diet consisting of 23% corn oil in order to increase tumor incidence in the distal colon [51]. At time points of ~18 weeks, the mice were prepared for imaging study. One day before imaging, the mice were injected with the cathepsin B-sensitive contrast agent (ProSense^{TM} 680, PerkinElmer), which was non-fluorescent at injection and locally activated after target interaction [52,53]. After 24 hours, animals were euthanized. For each animal, a 5-cm long section of colon from the distal end was removed, opened longitudinally, and flushed with isotonic saline. The excised colon was pinned flat and fixed using Formalin in place to minimize fixation artifacts. After fixation, the samples are ready for imaging. Photos of all the samples were taken using a digital camera and all the tumors were numbered properly, which would be used to match the measurements from OCT/FLOT with histology results.

2.2 System setup

Figure 1(A) shows the OCT system setup. This frequency-domain OCT imaging system utilized a wavelength-swept laser as light source which was centered at 1310 nm with 100 nm bandwidth [54]. The wavelength-swept frequency was 16 kHz with 17 mW output power [55]. About 97% of the laser power was split evenly to the sample and reference arms of a fiber-based Michelson interferometer [56, 57]. The signals reflected from the sample and reference arms formed interference fringes at the fiber couple (FC). The interference fringes from different depths received by a balanced detector (BD) were encoded with different frequencies. A Mach-Zehnder interferometer (MZI) obtained the remaining 3% of the laser output power and generated a frequency-clock signal with uniformly spaced optical frequency to trigger the sampling of the OCT signal [58]. Depth-resolved tomography can be achieved by performing fast Fourier transform of the interference fringes. During imaging, the colon tissue was irrigated by phosphate buffer saline (PBS) to prevent dehydration [59].

The schematic of the FLOT system is shown in Fig. 1(B). A 637 nm laser diode was utilized as light source. Light from the laser diode was collimated and coupled into a single-mode fiber to shape the light beam. Light coming out from the fiber was first collimated by an objective lens (O1) and then passed through a polarizer (P1). The collimated light was expanded into line-field illumination using a cylindrical lens with a full line-width at the half maximum of 26 μm at the focal plane. An iris was used to control the length of the line illumination. The backscattered light and emitted fluorescent light were collected back through a cross-polarizer (P2, which was used to reject the specular reflection from the sample surface), another objective lens (O2), a filter wheel (695 nm emission filter for fluorescence imaging and no filter for reflectance imaging), and finally imaged on a CCD camera (EM-CCD, CooKe). Recent studies indicated angled illumination and detection configurations can improve both resolution and depth sensitivity [42, 60]. The illumination angle was set at 45°, rendering ~30° transmission angle in tissue (n~1.33). The CCD camera was placed vertically to record both fluorescence and reflectance images by rotating the filter wheel. Because of the defocusing effect, we set the focal plane slightly below the sample surface. The scattering coefficient (μ_s) of the colon sample was determined from the reflectance data using oblique-incidence spectroscopy [61] to be ~146 cm^{-1}. A motorized stage was used to translate the sample laterally in scanning direction X (perpendicular to the line illumination direction Y) with the speed of 0.2156 mm/s.

Biomedical Optics EXPRESS

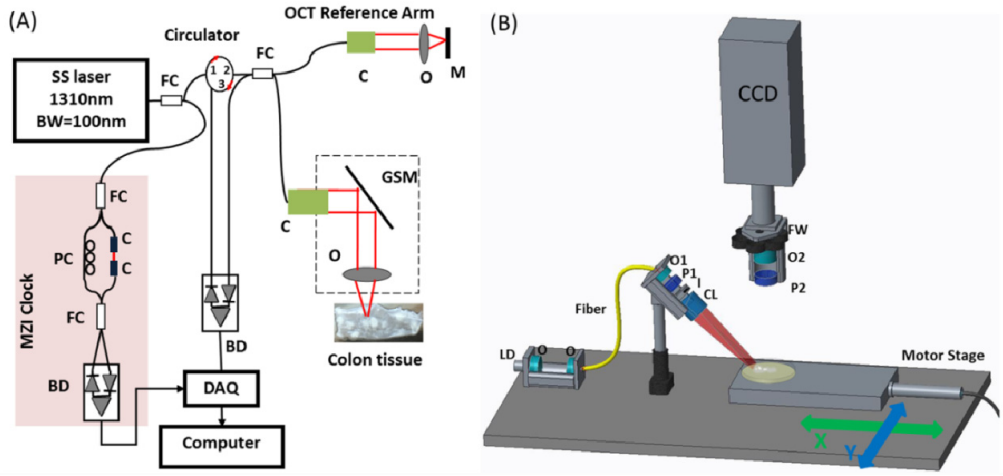

Fig. 1. (A) Schematic of the OCT imaging system. (B) Schematic of the FLOT system. FC: fiber coupler; PC: polarization controller; C: collimator, BD: balanced detector, MZI: Mach-Zehnder interferometer (frequency clocks), DAQ: data acquisition board, M: mirror, GSM: galvonometer scanning mirror, O: objective lens, LD: laser diode, P: polarizer, S: shutter, I: iris, CL: cylindrical lens, FW: filter wheel.

2.3 Data acquisition and reconstruction

For FLOT image acquisition, the illumination line was first focused on the border (X = 0) of the sample field of view (FOV). At each scanning position, one 2D XY image (512x512, with pixel dimension of 30.8 μm) was obtained with 100 ms exposure time. Next, the motorized stage moved the sample in X direction with a step size of 30.8 μm to another illumination/collection position. Another 2D XY data set was obtained. This process was repeated until finishing the entire sample scanning [42]. The raw measurement had the format of XYT. A typical 3D data set recorded 512 × 512 × 400 XYT voxels. In order to fit the experimental data to the theoretical model for precise reconstruction, the surface of colon tissue must be found. To obtain the surface tomography of the colon tissue, the emission filter was removed, and the same FOV was scanned to get the reflectance images with the same scanning/acquisition protocol but lower laser power to avoid saturated image. Without emission filter, most of the collected light was from the reflection of the illumination light at the tissue surface, which would then serve as an indicator of the location of tissue-air interface. The raw measurement of reflectance data set had exactly the same format of XYT (X = 512, Y = 512, T = 400).

To reconstruct the images, the 3D data sets were first downsized to 256 × 256 × 200 XYT voxels. The raw measurements of the reflectance data were stacked together according to the geometrical relationship between the illumination plane and the detection FOV, which was similar to the unprocessed stacked raw image in selective plane illumination microscopy [62]. Additionally, the stacked reflectance data were used to co-register with the 3D OCT data based on the shape / structural features of the same tumor. To reconstruct the fluorescence image, first-order Born approximation was assumed to obtain linearity between the measurement F and the fluorophore distribution C, i.e., for each FOV_{XZ}, F = JC, with J the weight or sensitivity matrix [42, 48]. To constitute J, photon distribution was first generated by Monte-Carlo simulation [63] (g = 0.9, n = 1.33, $\mu_a = 0.01 \times \mu_s$, $\mu_s = 146\ cm^{-1}$). Then the reciprocity principle was applied to obtain J.J was later decomposed by singular value decomposition (SVD) [64]. Lastly, least square fitting and Tikhonov regularization were used to solve the underdetermined system [60]. The regularization parameter $\alpha = 0.0021$ was determined by L-curve criterion [65]. 100 source-detector pairs and 100 scanning positions starting from the surface were chosen to constitute F with 10,000 measurement data. Each

Biomedical Optics EXPRESS

reconstructed FOV_{XZ} included 100 × 100 pixels with a pixel size of ~61.6 μm. The entire volume FOV_{XYZ} was constituted by juxtaposing individual FOV_{XZ} along Y-direction. After imaging, the pinned tissue specimens were processed for histology and pathological review (Histoserv, Inc).

2.4 Data quantification

To achieve quantitative characterization of tumors and normal tissues in mouse colon, the structural and molecular parameters can be extracted from OCT and FLOT images respectively. Tissue extinction coefficient (μ_t) (or the slope of axial attenuation) is an indication of local tissue scattering changes associated with neoplasia, and has been shown to be able to detect dysplasia in oral cavities [66, 67] and breast cancer [68, 69]. The extinction coefficient (μ_t) can be estimated by fitting the OCT axial-scan intensity profiles with the single-scattering model: $I(z) \propto \exp(-2*\mu_t*z)$ [70]. Since the extinction coefficient (μ_t) is the sum of the absorption coefficient (μ_a) and scattering coefficient (μ_s), the enhanced light attenuation in the tumor regions could be due to the increase of tissue scattering coefficient, which is closely related to the structural changes such as nuclear-to-cytoplasmic ratio and extracellular matrix remodeling during the neoplastic progression. Absorption coefficients might be also changed due to changes in water contents (such as in the case of edema). However, at 1300 nm, for typical GI tissues, the scattering coefficient is at least one order of magnitude larger than the absorption coefficient [71]. Therefore, the majority of attenuation could be due to scattering, i.e., $\mu_t \approx \mu_s$. We therefore quantified the scattering coefficient (μ_s) as the structural parameter.

Molecular parameters include the level and spatial distribution of enzyme (cathepsin B) activities, which can be quantified from the depth-resolved FLOT tomogram using cathepsin-B-activatable contrast agent. Depth-resolved FLOT is capable of reconstructing the intensity and depth distribution of the contrast agent (ProSense^{TM}680). To calibrate the constructed values to fluorophore concentrations, capillary tubes with 200 μm inner diameter and 330 μm outer diameter (Vitrocom. Inc) filled with different concentrations of fluorescence dye Cy5.5 (0.5 μM, 1 μM, 1.5 μM) were used as a calibration phantom. They were placed ~500 μm deep in the scattering medium containing 1.5 g Agar powder, 1 mL intralipid (20% solution), and 49 mL PBS buffer with μ_s~146 cm^{-1} at 637 nm, which is close to colon tissue scattering coefficient. The reconstructed relative enzyme activity value for 0.5 μM, 1 μM, 1.5 μM Cy5.5 were 207.66, 217.46 and 224.50 respectively revealing a good linear relationship with R^2 = 0.99113 which can serve as a good reference for the FLOT system used.

2.5 Data statistical analysis

According to the sample size calculation in the study plan, we recruited 17 samples in total (from 6 different animals) to ensure at least 80% power to detect the difference between tumor and normal tissues. No missing data are observed in this study. Descriptive statistics such as mean and standard deviation were calculated. The distributions of scattering coefficients μ_s and relative enzyme activity of tumor tissues to the normal tissues were examined to verify the normality assumption. Ratios of absolute diameter and thickness difference from OCT and FLOT to histology (gold standard) at different thresholds were compared to determine the optimal threshold values (the smaller the better). Boxplots are used to demonstrate the difference in parameters for tumor and normal tissues using OCT and FLOT. Student *t*-test was also used to compare the mean diameter and thickness from OCT and FLOT to histology at the chosen thresholds. Student *t*-test was used to compare scattering coefficient μ_s and relative enzyme activity of tumor tissues to the normal tissues. To quantify the diagnostic sensitivity and specificity for GI cancer detection using multi-modal OCT/FLOT imaging technologies and validate its capability for enhanced cancer detection compared to single modality alone, different thresholds of the tissue scattering coefficient (μ_s) (for OCT) and relative enzyme activity (for FLOT) were applied. To classify tumor tissue and

Biomedical Optics EXPRESS

normal tissue near tumor with combined OCT and FLOT results, linear discriminant analysis (LDA) was trained with relative enzyme activity and tissue scattering coefficient (μ_s) from the data sets plotting in X and Y dimensions respectively and applied to new testing samples. Receiver operations curve (ROC) was also used to assess the classification performance based on FLOT, OCT and the combined criteria. Statistical analyses were carried out using MATLAB (The MathWorks Inc., Natick, MA). Statistical significance is considered at $P = 0.05$.

3. Results and discussion

A representative 3D OCT colon tissue volume is shown in Fig. 2(A). The shape of colon tumor is clearly displayed. Figure 2(B) shows 3D FLOT image of the same colon tissue.

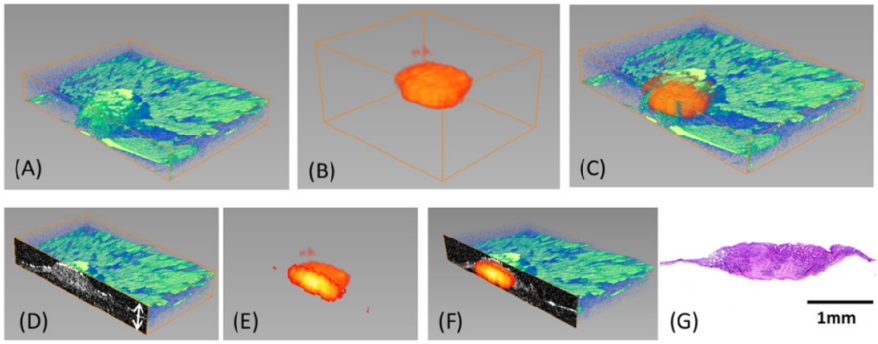

Fig. 2. (A) 3D OCT image (X × Y × Z = 5 × 3 × 0.5 mm^3). (B) 3D FLOT image (X × Y × Z = 3.8 × 3.3 × 2 mm^3). (C) 3D OCT and FLOT fused image. (D) Cross-sectional OCT images. (E) Cross-sectional FLOT images. (F) 2D OCT and FLOT fused image. (G) Corresponding histology

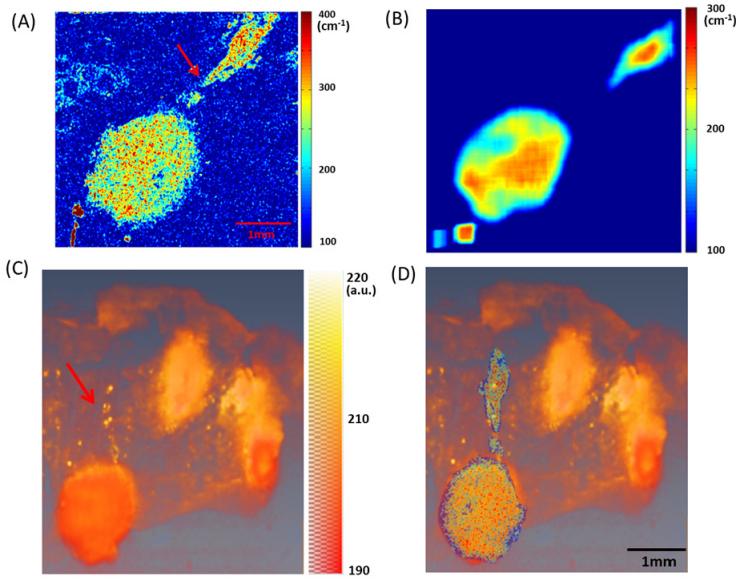

Fig. 3. (A) Tissue scattering coefficient (μ_s, cm^{-1}) image. (B) Tissue scattering coefficient (μ_s, cm^{-1}) image after sliding filtering. (C) Top view of FLOT 3D image using cathepsin B-sensitive fluorescent contrast agent. Relative enzyme activities are higher around tumor areas than the surrounding normal tissue. (D) Fused scattering coefficient and fluorescence image.

Biomedical Optics EXPRESS

These two 3D images agree well as shown in the fused 3D image (Fig. 2C). Figure 2(D) and 2(E) show the corresponding cross-sectional OCT and FLOT images. Due to the scattering effect, OCT signals attenuate at deeper regions, while FLOT can provide better depth information as shown in Fig. 2(F). Both data agree with the corresponding histology (Fig. 2G). These results clearly demonstrate the feasibility of OCT and FLOT for co-registered tissue morphology and molecular information, and the capability of FLOT to visualize the depth information of subsurface tumors.

3.1 Structural and molecular biomarkers

From Fig. 3(A), the colon tumor shows enhanced light attenuation compared to normal regions. The red arrow indicates the landmark we can use to co-register tissue scattering coefficient (μ_s) map with the top-down view of FLOT 3D image shown in Fig. 3(C). Our findings are consistent with previous animal study [59] and clinical observations of reduced OCT scattered light in adenomatous polyps of the human colon [72]. Another observation is the heterogeneity in the tumor region [73] as shown in Fig. 3(A). Figure 3(C) shows the top-down view of FLOT 3D image using fluorescent contrast agent. Colon adenomas show enhanced fluorescence compared to normal regions. Depth distribution of the contrast agent can be seen in Fig. 2(E). Figure 3(D) shows fused scattering coefficient and fluorescence image based on the landmark indicated by the red arrow. These parameters will indicate the level of molecular activities, size, and depth of invasion of the tumor.

3.2 Parameters for tumor size measurement

OCT/FLOT images provide the parameters to differentiate neoplastic lesions from normal tissues. We first applied these parameters to estimate the size of tumors to differentiate different stages of neoplastic lesions. For OCT, since the scattering coefficient (μ_s) map (Fig. 3A) is heterogeneous, in order to find the optimal threshold value for tumor size estimation, a sliding neighborhood operation with 100-by-100 sliding blocks was applied to the scattering coefficient (μ_s) map (1360 × 1240). The scattering coefficient (μ_s) map after sliding neighborhood operation is shown in Fig. 3(B). Then from the intensity profiles along both X and Y directions, the full-widths of the intersections with different threshold values were estimated as the tumor size (i.e., all the pixels with the same Y position were summed up when we calculate the intensity profile along X direction). The different threshold values were derived by the following equation: $(I_{max} - I_{min}) \times H\% + I_{min}$, where I_{max} is the maxium value and I_{min} is minimum value or the background value on the each specific intensity profile. $H\%$ are the different percentages that we can use to calculate different threshold values and the values for $H\%$ are set 30%, 40%, 50%, 60% and 70% in this study. The tumor diameter was determined by averaging two dimensional measurements (X and Y). Finally the absolute value of error function (the absolute diameter or thickness difference) $E = \dfrac{\text{Measure} - \text{Histoloy}}{\text{Histology}}$ was used to judge the accuracy of the measurement for different threshold values. Tissue scattering coefficient (μ_s) maps were obtained on 12 samples from 6 different animals. The statistics of the 12 samples with different threshold values is shown in Fig. 4(A). 60% threshold provided the best result (E = 0.323 ± 0.057). Tumor thickness was determined from OCT cross-sectional image as shown

Biomedical Optics EXPRESS

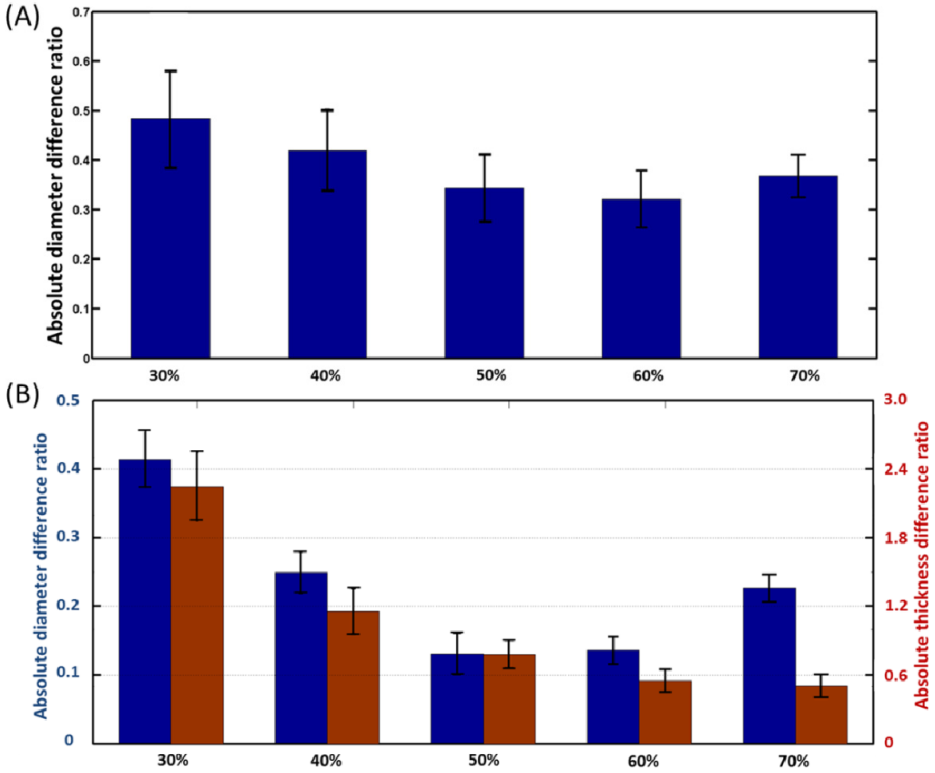

Fig. 4. (A) Average absolute diameter difference ratio for OCT with different threshold (n = 12, from 6 different animals). (B) Average absolute diameter and thickness difference ratio for FLOT with different threshold (n = 12, from 6 different animals).

in Fig. 2(D) (indicated by the white double-head arrow). For FLOT, we used the same protocol to determine the optimal threshold in tumor sizes in XYZ dimensions. The tumor diameter was determined by averaging two dimensional measurements (X and Y) for different threshold values. Tumor thickness was determined from the tumor size in Z dimension for different threshold values. As shown in Fig. 4(B), 50% threshold gave the best measurement (E = 0.131 ± 0.032) for tumor diameter but not the optimal measurement (E = 0.780 ± 0.191) for tumor thickness, while 60% threshold provided a comparatively good estimation (E = 0.135 ± 0.021) for tumor diameter but a markedly better measurement (E = 0.551 ± 0.102) for tumor thickness estimation. Thus we chose 60% threshold for FLOT data sets. Using the optimal thresholds we chose, the sizes from measurements were then plotted together with histology data which served as the gold standard as shown in Fig. 5. FLOT provides a more accurate estimation in tumor diameter (E = 0.135 ± 0.021) but relatively worse in thickness estimation (E = 0.551 ± 0.102) due to the inverse reconstruction nature of FLOT. OCT gives a better estimation in depth direction (E = 0.264 ± 0.045) since there is colon serosa below tumor which scatters more light back than tumor tissue, and serves as the lower tumor boundary.

Biomedical Optics EXPRESS

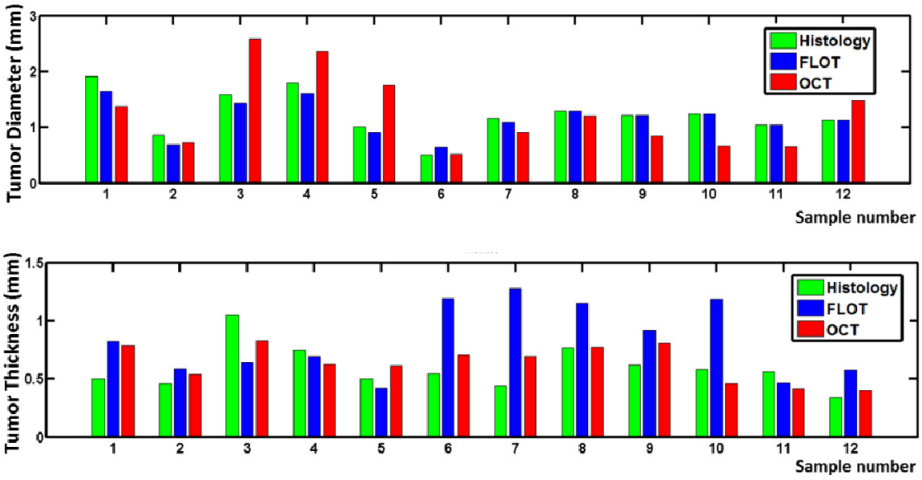

Fig. 5. Diameter and thickness from FLOT and OCT compared to histology (n = 12, from 6 different animals).

While we can notice that OCT signals attenuate at deeper regions, the tumor thickness is mainly based on tissue surface height (with respect to a fixed reference position), and in our case, the tumor region is comparably thicker than the normal tissue. That may result in more accurate thickness estimation from OCT in this experiment, but for *in vivo* case, the accuracy of tumor thickness estimation may not be that precise. Even though FLOT's estimation is not ideal for tumor thickness, it is still able to estimate the depth within certain accuracy ranges (~50%), which can provide additional information compared to 2D fluorescence imaging method or simple white light examination. For diameter estimation, since we used tissue scattering coefficient (μ_s) to determine the size, both the anisotropy and heterogeneity of the tumor region may result in inaccurate ($E = 0.323 \pm 0.057$) measurement compared to the actual size of the tumor determined by histology. By taking advantage of the two imaging methods, there is a great potential to obtain tumor sizes in all dimensions in order to differentiate different stages of neoplastic lesions. We tried to perform the histology in the middle line of each tumor, so the diameter and thickness data should be able to reflect the dimensions of each tumor. However, using markers will definitely provide better correlation between two imaging methods and histology and more accurate results [74].

3.3 Parameters for tumor detection

To quantify the parameters mentioned above in differentiating colon tumor and tissues nearby tumor, tissue scattering coefficient (μ_s) and relative enzyme activity were determined by averaging the values of randomly picked 5 × 5 pixels region of interest (ROI) in tumor and normal tissues near tumor on 17 samples from 6 different animals (the tumor area was determined using the optimal threshold derived in *Section 3.2*). There are in total 68 data sets (2 data sets were taken from each tumor region and 2 data sets were taken from each normal tissue near tumor.). As shown in the left part of Fig. 6, the tissue scattering coefficient (μ_s) of the tumor region is statistically larger than the control group ($P<0.001$). The relative enzyme activity of tumor region as shown in the right part of Fig. 6 is statistically larger than that of normal tissue as well ($P<0.001$). The tissue scattering coefficient (μ_s) is relatively lager than the values previously reported [75, 76]. This increase may originate from formalin fixation since it has been reported that formalin fixation can result in increasing scattering coefficient due to the cross-linking of proteins creating a more highly scattering media [77, 78].

Biomedical Optics EXPRESS

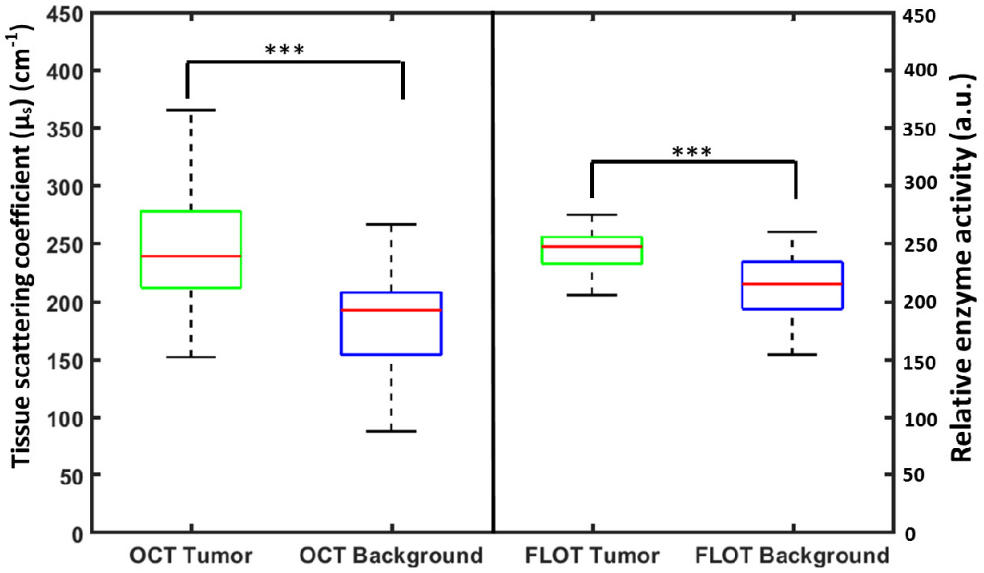

Fig. 6. Statistics of tissue scattering coefficient (μ_s) and Relative enzyme activities in tumor tissue and normal tissue near tumor. The tissue scattering coefficient (μ_s) of the group of tumor tissue (n = 34, from 6 different animals) was statistically ($P<0.05$) bigger compared to control group (normal tissue near tumor: n = 34, from 6 different animals). The relative enzyme activity in the group of tumor tissue was statistically ($P<0.05$) larger than control group.

3.4 Diagnostic accuracy of combined imaging modalities

The tissue scattering coefficient (μ_s) and relative enzyme activity were determined by averaging the values of randomly picked 5 × 5 pixels ROI in tumor and normal tissue near tumor on 17 samples from 6 different animals. There are in total 68 data sets (2 data sets were taken from each tumor region and 2 data sets were taken from each normal tissue near tumor). Relative enzyme activity and tissue scattering coefficient (μ_s) from the data sets are plotted in X and Y dimensions respectively as shown in Fig. 7(A). LDA found the best separation of the two groups (tumor and normal tissues near tumor) as shown in Fig. 7(A). Figure 7(B) shows the ROC curves for diagnosis using tissue scattering coefficient only and relative enzyme activity only, and the corresponding optimal diagnostic sensitivity and specificity using the combined criteria. The optimal sensitivity (specificity) for scattering coefficient only is 76.47% (82.35%), relative enzyme activity only is 85.29% (70.59%), and combined criterion is 82.35% (82.35%). Combined criterion gives the optimal diagnosis (i.e., the shortest distance to ideal diagnosis 100% (100%)). Fluorescence molecular imaging can achieve high sensitivity in detecting early cancer, however, has limited specificity due to confounding factors such as inflammation.

Biomedical Optics EXPRESS

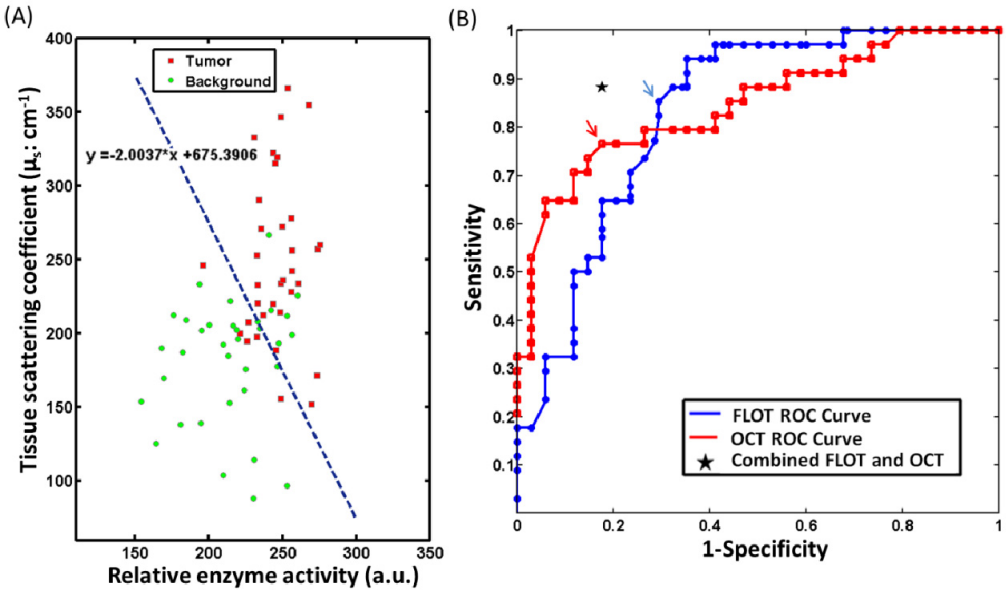

Fig. 7. (A) LDA for classification of tumor tissue and normal tissue near tumor;(B) ROC curves for using tissue scattering coefficient only, relative enzyme activity only, and combined criteria. The arrows indicated the optimal threshold for OCT and FLOT. Combined criterion gives the optimal diagnosis (i.e., the closest distance to ideal diagnosis 100% (100%)).

On the other hand, OCT is less sensitive to early neoplastic changes before significant structural alterations occur, but has high specificity to rule out the non-neoplastic regions. Combined together, fluorescence molecular imaging and OCT can provide complementary information for more accurate detection and characterization of early neoplasia.

To validate the combined criteria, another 68 data sets were collected from the 17 samples, as the validation data set, to determine the sensitivity and specificity of the criteria value in an independent study. With the diagnostic threshold of $y = -2.0037 \times x + 675.3906$ derived in Fig. 7(A), the sensitivity (specificity) for validation data was 88.23% (82.35%) compared to 79.41% (82.35%) for OCT only and 85.29% (73.52%) for FLOT only. We should notice that cathepsin B-sensitive contrast agent used in the paper may not be optimal for tumor cell targeting. FLOT is a general method and can work with other contrast agents. In the future, cyclic Arg-Gly-Asp (RGD) [79], folate receptor-α [80], and affinity peptide [81] can be considered to further improve the diagnostic accuracy.

4. Conclusion

We investigated a multi-modal optical imaging approach combining high-resolution OCT and depth-resolved high-sensitivity FLOT for structural and molecular imaging. Quantitative structural (scattering coefficient) and molecular (relative enzyme activity) parameters from OCT/FLOT images were derived for multi-parametric analysis. This multi-modal imaging method has demonstrated the feasibility for more accurate diagnosis with 88.23% (82.35%) for sensitivity (specificity) which gives the optimal diagnosis compared to each individual imaging modality. This new multi-modal imaging technology is able to provide comprehensive structural and molecular parameters for better assessment of subsurface lesions. Therefore, such an imaging technology could detect subsurface cancers and pre-cancers to improve the diagnostic sensitivity, monitor the neoplastic progression underneath the surface, and assess the efficacy of ablative therapies. Integrated OCT and line-scan FLOT has been demonstrated through a dichroic mirror [58]. In the future, we will combine high-

Biomedical Optics EXPRESS

resolution OCT and depth-resolved high-sensitivity FLOT into one imaging system for more studies on different disease models, which can provide co-registered structural and molecular information of tissues simultaneously. The two imaging modalities could be further integrated into a functional endoscopy system using microelectromechanical system (MEMS), GRIN cylindrical lens (GRINTECH. Inc), and imaging fiber bundle [82]. Since Monte Carlo modeling and regularization term are applied in reconstructing FLOT images, it is time-consuming and cannot provide the reconstructed image in real time especially for a system with high source–detector density. But with the advent of the computer speed and new regularization methods introduced [83], the time needed for image reconstruction in FLOT could be alleviated dramatically.

Funding

National Institutes of Health (NIH) (R21EB012215-01A1, R01EB014946-01A1).

Acknowledgement

We thank Joanne May Chan from University of Maryland for data analysis and discussion.